



Measuring the H I Content of Individual Galaxies Out to the Epoch of Reionization with [C II]

Kasper E. Heintz^{1,2} , Darach Watson² , Pascal A. Oesch^{2,3} , Desika Narayanan^{2,4,5} , and Suzanne C. Madden⁶

¹ Centre for Astrophysics and Cosmology, Science Institute, University of Iceland, Dunhagi 5, 107 Reykjavík, Iceland; keheintz@hi.is

² Cosmic Dawn Center (DAWN), Niels Bohr Institute, University of Copenhagen, Jagtvej 128, DK-2100 Copenhagen Ø, Denmark

³ University of Geneva, Department of Astronomy, Chemin Pegasi 51, 1290 Versoix, Switzerland

⁴ Department of Astronomy, University of Florida, 211 Bryant Space Sciences Center, Gainesville, FL 32611 USA

⁵ University of Florida Informatics Institute, 432 Newell Drive, CISE Bldg E251, Gainesville, FL 32611, USA

⁶ AIM, CEA, CNRS, Université Paris-Saclay, Université Paris Diderot, Sorbonne Paris Cité, F-91191 Gif-sur-Yvette, France

Received 2021 May 24; revised 2021 August 9; accepted 2021 August 26; published 2021 November 26

Abstract

The H I gas content is a key ingredient in galaxy evolution, the study of which has been limited to moderate cosmological distances for individual galaxies due to the weakness of the hyperfine H I 21 cm transition. Here we present a new approach that allows us to infer the H I gas mass M_{HI} of individual galaxies up to $z \approx 6$, based on a direct measurement of the [C II]-to-H I conversion factor in star-forming galaxies at $z \gtrsim 2$ using γ -ray burst afterglows. By compiling recent [C II]-158 μm emission line measurements we quantify the evolution of the H I content in galaxies through cosmic time. We find that M_{HI} starts to exceed the stellar mass M_* at $z \gtrsim 1$, and increases as a function of redshift. The H I fraction of the total baryonic mass increases from around 20% at $z = 0$ to about 60% at $z \sim 6$. We further uncover a universal relation between the H I gas fraction M_{HI}/M_* and the gas-phase metallicity, which seems to hold from $z \approx 6$ to $z = 0$. The majority of galaxies at $z > 2$ are observed to have H I depletion times, $t_{\text{dep,HI}} = M_{\text{HI}}/\text{SFR}$, less than ≈ 2 Gyr, substantially shorter than for $z \sim 0$ galaxies. Finally, we use the [C II]-to-H I conversion factor to determine the cosmic mass density of H I in galaxies, ρ_{HI} , at three distinct epochs: $z \approx 0$, $z \approx 2$, and $z \approx 4-6$. These measurements are consistent with previous estimates based on 21 cm H I observations in the local universe and with damped Ly α absorbers (DLAs) at $z \gtrsim 2$, suggesting an overall decrease by a factor of ≈ 5 in $\rho_{\text{HI}}(z)$ from the end of the reionization epoch to the present.

Unified Astronomy Thesaurus concepts: High-redshift galaxies (734); Interstellar medium (847); Gamma-ray bursts (629); Galaxy evolution (594)

1. Introduction

The first epoch of galaxy formation is governed by the infall of pristine gas. These reservoirs of neutral gas are composed mostly of atomic hydrogen (H I), which then cools and condenses into molecular gas and initiates star formation. The H I gas content is therefore a key ingredient in galaxy evolution. In the local universe the hyperfine H I 21 cm transition has been used as the main tracer of this neutral atomic gas (Zwaan et al. 2005; Hoppmann et al. 2015; Jones et al. 2018), but due to the weakness of the line this approach is only feasible out to $z \approx 0.4$ for individual galaxies (Fernández et al. 2016).

Similarly, cold molecular hydrogen (H_2) is difficult to detect in emission due to its lack of a permanent dipole moment. The recent advent of facilities operating at submillimeter wavelengths such as the Atacama Large Millimeter/submillimeter Array (ALMA), however, have enabled exploration of the dusty and molecular gas-phases of galaxies through proxies such as carbon monoxide (CO; Tacconi et al. 2010; Bolatto et al. 2013), neutral atomic carbon ([C I]; Papadopoulos et al. 2004; Walter et al. 2011; Valentino et al. 2018), ionized carbon (C II; Zanella et al. 2018; Madden et al. 2020), and dust (Magdis et al. 2012; Scoville et al. 2014, 2016), which have all been employed as effective tracers of the molecular gas (see also Tacconi et al. 2020; Valentino et al. 2020; Harrington et al. 2021). The weakness of the hyperfine 21 cm transition of H I and the crucial importance of H I as the fuel for galaxy evolution, similarly demands a powerful alternative that can probe the neutral atomic H I gas content in the most distant galaxies.

Here we develop a calibration similar to those utilized in high-redshift galaxy surveys targeting the CO or [C I] transitions to infer the total molecular or H_2 gas mass, but instead calibrated to H I. The [C II]-158 μm fine-structure transition, often the brightest atomic or ionic line emitted from galaxies, is an attractive candidate for such a calibration. This line originates primarily from the cold, neutral gas so finding a way to calibrate it to trace the overall H I gas content is an important goal. While the line has previously been used as a proxy for the molecular gas content of galaxies (Zanella et al. 2018; Madden et al. 2020), observations (Pineda et al. 2014; Croxall et al. 2017; Díaz-Santos et al. 2017; Cormier et al. 2019; Tarantino et al. 2021) and simulations (Franeck et al. 2018; Pardos Olsen et al. 2021; Ramos Padilla et al. 2021) show that typically the molecular phases make only a minor contribution to the total [C II] line luminosity. The association of the [C II]-158 μm line with the diffuse ionized or neutral atomic gas is further supported by the extent of its emission being greater than the star-forming disk, the CO component, and the dust continuum in both low- and high-redshift galaxies (Madden et al. 1997; Carniani et al. 2018; Fujimoto et al. 2019; Harikane et al. 2020; Herrera-Camus et al. 2021). A significant fraction of the [C II] emission is therefore proposed to originate from the extended interstellar gas disk of galaxies. Determining the [C II]-to-H I conversion factor thus provides a unique approach to probing the H I gas content in individual galaxies.

The approach presented here does not rely on any scaling relations or assumptions about the physical state of the gas. The [C II]-to-H I calibration is derived purely from direct measurements

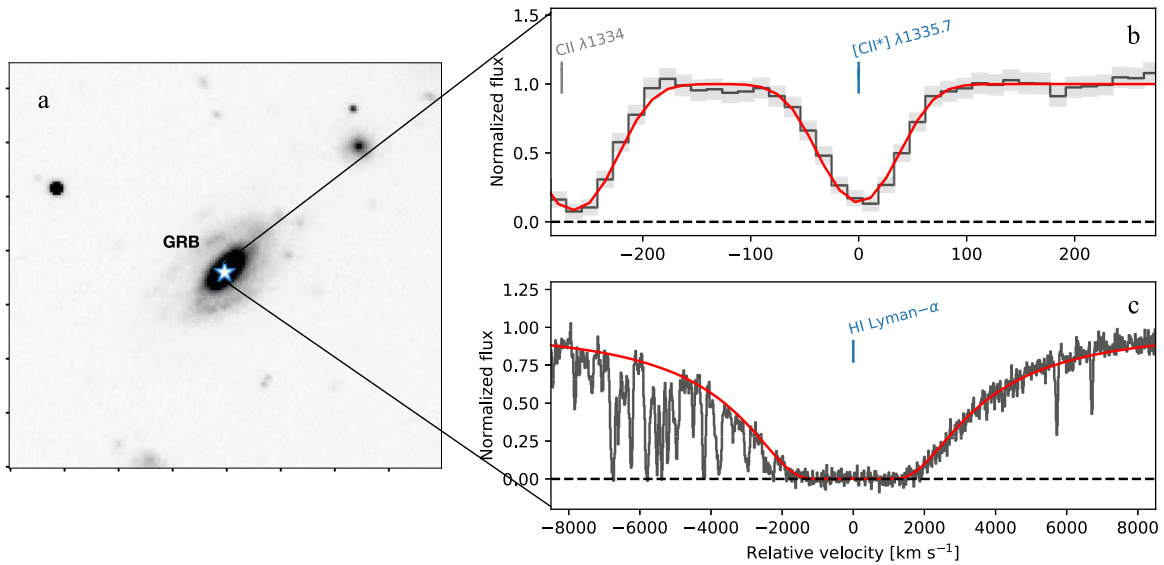


Figure 1. Illustration of GRBs as probes of the ISM in their hosts. Panel a shows the typical explosion sites of GRBs, close to the center or brightest regions of their host galaxies. Panels b and c show examples of absorption features from $[\text{C II}]^* \lambda 1335.7$ and $\text{H I Ly}\alpha$ imprinted on the optical afterglow spectrum of one of the sample GRBs, GRB 090926A. Any velocity components of $[\text{C II}]^* \lambda 1335.7$, representing individual gas complexes along the line of sight, are typically resolved in wavelength space. The high abundance of H I visualizes as a single broad absorption trough. We use a sample of 15 GRB afterglows with good-quality spectra to determine the $[\text{C II}]^*$ and H I content.

of the relative abundances in the line of sight through the interstellar medium (ISM) of galaxies hosting γ -ray bursts (GRBs). This approach does therefore not necessarily require the $[\text{C II}]$ -emitting gas to be physically associated with or predominantly originate in the H I gas reservoirs, but only provides an average abundance ratio of the two throughout the ISM. We present the GRB sample and outline the methodology used to derive the $[\text{C II}]$ -to- H I conversion factor in Section 2. In Section 3 we describe the sample compilation of $[\text{C II}]$ -emitting galaxies at $z \gtrsim 2$ and quantify the evolution of the H I gas mass content in galaxies from $z \approx 6$ to the present. In Section 4 we apply the $[\text{C II}]$ -to- H I conversion to determine the comoving mass density of H I in galaxies as a function of redshift $\rho_{\text{HI}}(z)$ based on the luminosity functions of $[\text{C II}]$. We provide a summary of our results in Section 5 and reflect on the future outlook of studying the H I content of high-redshift galaxies.

2. High-redshift $[\text{C II}]$ -to- H I Conversion

2.1. European Southern Observatory Very Large Telescope/X-shooter Observations

The bright optical afterglows of GRBs can serve as powerful background sources to probe the various gas-phase constituents of the ISM in their host galaxies (Jakobsson et al. 2004; Fynbo et al. 2006; Prochaska et al. 2007). Since long-duration GRBs are linked to the death of massive stars (Woosley & Bloom 2006), they are expected to trace star formation through cosmic time (Robertson & Ellis 2012; Tanvir et al. 2012; Greiner et al. 2015; Perley et al. 2016). Most GRB afterglow spectra are characterized by a broad absorption trough from the $\text{H I Ly}\alpha$ transition (Vreeswijk et al. 2004; Jakobsson et al. 2006; Fynbo et al. 2009), in line with being located behind a significant column of neutral gas in star-forming regions. Here we utilize the accurate abundances of H I and $[\text{C II}]^* \lambda 1335.7$, and the gas-phase metallicities, that can be derived in the line of sight through the ISM of GRB host galaxies to determine an empirical, metallicity-dependent $[\text{C II}]$ -to- H I conversion factor in high-redshift galaxies. This is illustrated in Figure 1.

This work is primarily based on the X-shooter GRB (XS-GRB) afterglow legacy survey (Selsing et al. 2019). This sample includes a set of carefully selected bursts detected by the Neil Gehrels Swift Observatory (Gehrels et al. 2004) during a ≈ 10 yr period. The sample criteria are constructed such that the observed sample provides an unbiased representation of the underlying population of Swift-detected bursts, while simultaneously optimizing the observability. We consider all GRB afterglows suitable to measure the column densities of the $\text{H I Ly}\alpha$ and $[\text{C II}]^* \lambda 1335.7$ transitions, effectively requiring that the bursts occurred in galaxies at $z \gtrsim 2$. This corresponds to the wavelength range above which $\text{Ly}\alpha$ is observable from the ground due to the atmospheric cutoff at shorter wavelengths. The spectra are further required to have signal-to-noise ratios (S/Ns) in the wavelength region encompassing the two transitions of $\text{S/N} \gtrsim 3$ to obtain reliable column density estimates. The final GRB afterglow sample considered in this work consists of the 15 bursts presented in Table 1. While biases in how GRBs trace star-forming galaxies might be inherent at low redshifts (Perley et al. 2016; Palmerio et al. 2019), they have been demonstrated to be reliable tracers of star formation (Robertson & Ellis 2012; Greiner et al. 2015) and sample the underlying star-forming galaxy population (Perley et al. 2016) at $z > 2$.

The GRBs in this sample probe galaxies spanning redshifts from $z = 2.11$ (GRB 090926A) to $z = 4.99$ (GRB 111008A). For each system, we adopt the H I column densities and dust-corrected metallicities derived by Bolmer et al. (2019). The latter is computed from a range of metal species X tracing the neutral interstellar medium. The relative abundances for each element are derived as $[\text{X}/\text{H}] \equiv \log(N(\text{X})/N(\text{H})) - \log(\text{X}/\text{H})_{\odot}$, with $(\text{X}/\text{H})_{\odot}$ representing solar abundances (Asplund et al. 2009). Since a fraction of the metals in the ISM are depleted by condensation onto interstellar dust grains, these are taken into account by correcting for the observed depletion level $[\text{X}/\text{Y}]$, which is also correlated with the metallicity of the galaxy (De Cia et al. 2016). This provides an estimate of the total, dust-corrected metallicity $[\text{X}/\text{H}] + [\text{X}/\text{Y}] = [\text{M}/\text{H}]$, hence denoted

Table 1
GRB Line-of-sight H I and [C II*] λ 1335.7 Column Densities and Metal Abundances

GRB	z_{GRB}	$\log N_{\text{HI}}$ (cm^{-2})	$\log N_{[\text{CII}^*]}$ (cm^{-2})	$\log(Z/Z_{\odot})$	$\log(\beta_{\text{CII}})$ (M_{\odot}/L_{\odot})
090809A	2.7373	21.48 ± 0.07	15.30 ± 0.39	-0.46 ± 0.15	2.25 ± 0.40
090926A	2.1069	21.58 ± 0.01	14.67 ± 0.04	-1.72 ± 0.05	2.98 ± 0.04
100219A	4.6676	21.28 ± 0.02	14.87 ± 0.13	-1.16 ± 0.11	2.48 ± 0.13
111008A	4.9910	22.39 ± 0.01	16.01 ± 0.23	-1.79 ± 0.10	2.45 ± 0.23
120327A	2.8143	22.07 ± 0.01	15.61 ± 0.47	-1.34 ± 0.02	2.53 ± 0.47
120716A	2.4874	21.73 ± 0.03	15.81 ± 0.31	-0.57 ± 0.08	1.99 ± 0.31
120815A	2.3582	22.09 ± 0.01	15.02 ± 0.08	-1.23 ± 0.03	3.14 ± 0.08
120909A	3.9290	21.82 ± 0.02	16.01 ± 0.26	-0.29 ± 0.10	1.88 ± 0.26
121024A	2.3005	21.78 ± 0.02	14.99 ± 0.24	-0.68 ± 0.07	2.86 ± 0.24
140311A	4.9550	22.30 ± 0.02	15.02 ± 0.54	-2.00 ± 0.11	3.35 ± 0.54
151021A	2.3297	22.14 ± 0.03	15.87 ± 0.50	-0.97 ± 0.07	2.34 ± 0.50
151027B	4.0650	20.54 ± 0.07	14.62 ± 0.06	-0.59 ± 0.27	1.99 ± 0.09
160203A	3.5187	21.74 ± 0.02	15.10 ± 0.31	-0.92 ± 0.04	2.71 ± 0.31
161023A	2.7100	20.95 ± 0.01	14.79 ± 0.01	-1.05 ± 0.04	2.23 ± 0.01
170202A	3.6456	21.53 ± 0.04	15.19 ± 0.24	-1.02 ± 0.13	2.41 ± 0.24

Note. The H I column densities and dust-corrected gas-phase metallicities are from Bolmer et al. (2019). [C II*] λ 1335.7 column densities are derived in this work. β_{CII} denotes the [C II]-to-H I conversion factor per unit column derived for each system.

as $\log(Z/Z_{\odot})$. The GRB sample probes galaxies with H I column densities in the line of sight in excess of $N_{\text{HI}} = 2 \times 10^{20} \text{ cm}^{-2}$, classifying them as damped Ly α absorbers (Wolfe et al. 2005), and relative abundances ranging from $\log(Z/Z_{\odot}) = -2.0$ to $\log(Z/Z_{\odot}) = -0.3$ (i.e., gas-phase metallicities of 1%–50% solar).

2.2. Absorption-line Fitting

In this work we determine the column densities of the fine-structure [C II*] λ 1335.7 transition for each system. Since C II traces the same neutral interstellar gas as several other, typically weaker transitions of other singly ionized elements such as Fe II, Zn II, Si II, and S II, these are used to guide the velocity structure, number of components, and broadening parameter when fitting the [C II*] λ 1335.7 line complex. The absorption-line profiles are modeled using VoigtFit (Krogager 2018), which simultaneously fits a set of Voigt profiles to the observed absorption features and provides the redshift z_{abs} , column density N , and broadening parameter b as output. For this procedure, the intrinsic line profiles are first deconvolved by the measured spectral resolution of each afterglow spectrum. For systems where multiple velocity components are detected, representing individual gas complexes along the line of sight, the sum of the individual column densities is reported. This is to be consistent with the procedure used to measure the H I abundances and gas-phase metallicities. The resulting column densities $N_{[\text{CII}^*]}$ are listed in Table 1. We emphasize here that the velocity structure of [C II*] λ 1335.7 in individual systems matches well the elements tracing the neutral gas-phase, and not the typical single components observed for H₂ or [C I] (Bolmer et al. 2019; Heintz et al. 2019), further supporting the physical connection between [C II] and H I.

2.3. [C II]-to-H I Calibration

The line transition [C II*] λ 1335.7, typically observed in quasar damped Ly α absorbers (DLAs; Wolfe et al. 2003; Neeleman et al. 2015) and GRB (Fynbo et al. 2009; Christensen et al. 2011) absorption spectra, arises from the $^2P_{3/2}$ level in the

ground state of ionized carbon (C⁺). Determining the column density of this particular feature ($N_{[\text{CII}^*]}$) thus provides a measure of the C⁺ in the $J=3/2$ state along the line of sight. The population in this state gives rise to the [C II]-158 μm transition ($^2P_{3/2} - ^2P_{1/2}$). This allows us to determine the line's column luminosity $L_{[\text{CII}]}$, i.e., the luminosity per unit area, based on the spontaneous decay rate, as $L_{[\text{CII}]}^c = h\nu_{\text{ul}}A_{\text{ul}}N_{[\text{CII}^*]}$. For [C II]-158 μm , $\nu_{\text{ul}} = 1900.537 \text{ GHz}$ and $A_{\text{ul}} = 2.4 \times 10^{-6} \text{ s}^{-1}$. Similarly, the line-of-sight H I column mass density can be determined, $M_{\text{HI}}^c = m_{\text{HI}}N_{\text{HI}}$, where m_{HI} is the mass of a single hydrogen atom and N_{HI} is total H I column number density. This yields an expression for the line-of-sight [C II]-to-H I conversion factor in terms of the measured column densities $\beta_{[\text{CII}]} \equiv M_{\text{HI}}/L_{[\text{CII}]} = M_{\text{HI}}^c/L_{[\text{CII}]}^c = m_{\text{HI}}N_{\text{HI}}/(h\nu_{\text{ul}}A_{\text{ul}}N_{[\text{CII}^*]})$. Assuming that the ratio of the derived column densities for each sightline is representative of the mean of the relative total population, $N_{\text{HI}}/N_{[\text{CII}^*]} = \Sigma_{\text{HI}}/\Sigma_{[\text{CII}^*]}$, the $\beta_{[\text{CII}]}$ calibration derived per unit column is thus equal to the global [C II]-to-H I conversion factor. This scaling is derived for each GRB in the sample and converted to solar units, M_{\odot}/L_{\odot} . Moreover, the absorption lines in GRB afterglow spectra also allow for very accurate measurements of the gas-phase metallicity to be made. We note that the column density of [C II*] λ 1335.7 has previously been used to estimate the total [C II] luminosity of a DLA galaxy (Simcoe et al. 2020), though based on strong assumptions about the geometry of the system.

The conversion from the column density ratio to typical units of M_{\odot}/L_{\odot} can be expressed as a constant scaling $M_{\text{HI}}/L_{[\text{CII}]} = N_{\text{HI}}/N_{[\text{CII}^*]} \times 1.165 \times 10^{-4} M_{\odot}/L_{\odot}$. We wish to emphasize here that a similar approach to determine the [C I]- and CO-to-H₂ ratio in absorption-selected galaxies was demonstrated to be able to reproduce equivalent conversion factors observed in emission and expected from hydrodynamical simulations (Heintz & Watson 2020), lending further credibility to this method. Moreover, this approach does not necessarily require the [C II]-158 μm emission to physically trace the H I gas, it simply provides a measure of the total H I gas and [C II*] abundance in the line of sight, the latter also being partially produced in molecular clouds and photodissociation regions (PDRs). Finally, our approach does not determine the global

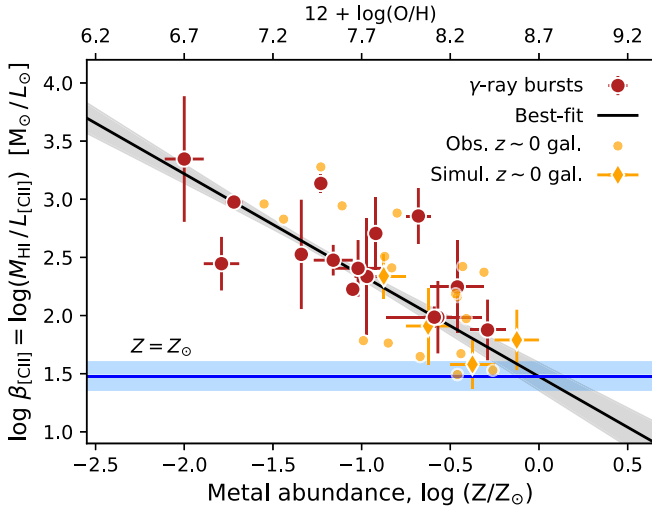


Figure 2. Absorption-derived metallicity evolution of the H I gas mass to [C II] line luminosity. The red symbols show the measured relative column densities of H I Ly α and [C II] λ 1335.7 in the line of sight, converted to units of M_{\odot}/L_{\odot} for each GRB. The gas-phase metal abundances have been measured from absorption lines and are corrected for dust. The black solid line and gray shaded region represent the best-fit linear relation and associated uncertainty. The blue solid line and shaded region mark the extrapolated [C II]-to-H I conversion factor β_{CII} at solar metallicities, $\beta_{\text{CII}} = 30^{+10}_{-7} M_{\odot}/L_{\odot}$. For comparison, the orange dots show the relative [C II] luminosity to H I gas mass inferred from 21 cm observations of galaxies at $z \sim 0$ and the orange diamond symbols show the average $M_{\text{HI}}/L_{\text{CII}}$ ratios in metallicity bins of 0.25 dex for a set of simulated galaxies at $z \sim 0$ (see the text).

properties for the GRB-selected galaxies, only the relative mass-to-luminosity ratio of H I and [C II], respectively. This scaling, however, can be applied to infer the global H I gas content of a given galaxy based on the total integrated luminosity of the [C II] emission line. This is the methodology used throughout this work.

Figure 2 shows the measured [C II]-to-H I relative abundances as a function of gas-phase metallicity, including the best-fit scaling relation between the two. The conversion factor, $\beta_{\text{CII}} = M_{\text{HI}}/L_{\text{CII}}$, is found to be linearly dependent on the metallicity, described by the following relation

$$\log M_{\text{HI}} = (-0.87 \pm 0.09) \times \log(Z/Z_{\odot}) + (1.48 \pm 0.12) + \log L_{\text{CII}}, \quad (1)$$

where Z/Z_{\odot} is the relative solar abundance (with $12 + \log(\text{O}/\text{H})_{\odot} = 8.69$ for $\log(Z/Z_{\odot}) = 0$; Asplund et al. 2009), and M_{HI} and L_{CII} are in units of M_{\odot} and L_{\odot} , respectively.

The observed scatter is likely dominated by variations in the physical properties of the ISM (such as density and gas pressure) and the intensity of the ultraviolet (UV) background field (Popping et al. 2019). For comparison, we overplot the sample of galaxies at $z \sim 0$ from the *Herschel* Dwarf Galaxy Survey (Madden et al. 2013), for which [C II] luminosities and H I gas masses from direct 21 cm observations have been inferred (see Rémy-Ruyer et al. 2014; Cormier et al. 2015, and references therein). We here only consider the main-sequence galaxies from this sample (within 0.5 dex), as parametrized by Speagle et al. (2014), to be consistent with the main analysis described in Section 3. Additionally, we include the average $M_{\text{HI}}/L_{\text{CII}}$ ratios of a set of $z \sim 0$ simulated galaxies shown in metallicity bins of 0.25 dex based on the simulations of Pardos Olsen et al. (2021). These theoretical expectations and the $z \sim 0$

galaxy sample are observed to match well with the empirical linear relation of β_{CII} as a function of metallicity observed for the GRB sample at $z > 2$, indicating a strong universal connection between the two.

The same analysis and results could in principle also be reproduced for DLAs originating in foreground galaxies toward bright background quasars. However, since quasar-selected DLAs are typically observed at high impact parameters (Péroux et al. 2011; Krogager et al. 2012; Christensen et al. 2014; Rahmani et al. 2016; Krogager et al. 2017), they mostly probe the extended H I envelope rather than the gas directly responsible for star formation in their associated galaxies (Neeleman et al. 2019). At these high impact parameters, the [C II] emission may be shock-heated intergalactic gas (Appleton et al. 2013) rather than excited by star formation. As a consequence, the observed [C II] λ 1335.7 contribution is likely to be much lower per unit of H I gas mass. Indeed, our preliminary analysis of quasar DLAs show on average a factor of ≈ 10 lower [C II] column luminosity per unit of H I column mass. DLA galaxy counterparts also show suppressed star formation compared to the main sequence of star-forming galaxies at equivalent redshifts (Rhodin et al. 2018), indicating that quasar DLA gas is not typically representative of the gas in star-forming galaxies.

3. Results

For the [C II]-to-H I conversion factor to be applicable to high-redshift galaxies, it is important that representative galaxy samples with high-quality auxiliary data are surveyed. For this work, we use recent sample compilations of [C II]-emitting galaxies at two distinct epochs: $z \sim 2$ and $z \sim 4-6$. These epochs are mainly defined by the redshifted frequency of the [C II]-158 μm transition observable by the available ALMA bands. Starbursts and quasar host galaxies are excluded in this analysis, such that only main-sequence star-forming galaxies are considered (see specific references below). Auxiliary data for each galaxy are further required, at minimum measurements of the star formation rate (SFR) and M_{\star} . These measurements are used to infer the gas-phase metallicity of each galaxy from the recent calibration of the fundamental metallicity relation (FMR; Curti et al. 2020). This is parametrized as

$$Z(M_{\star}, \text{SFR}) = Z_0 - \gamma/\beta \log(1 + (M_{\star}/M_0(\text{SFR}))^{-\beta}) \quad (2)$$

where $M_0(\text{SFR}) = 10^{m_0} \times \text{SFR}^{m_1}$, where we adopt their best-fitting parameters considering the total SFR: $Z_0 = 8.779$, $m_0 = 10.11$, $m_1 = 0.56$, $\gamma = 0.31$, and $\beta = 2.1$. Gas-phase metallicities for each galaxy are required to accurately determine the H I gas mass (Equation (1)). While the FMR is not well established at $z > 3$, the average metallicities inferred for the high-redshift samples described below reproduce the expected decrease of $\Delta \log(Z/Z_{\odot}) = -0.1$ per unit of redshift observed for star-forming galaxies up to $z \approx 3.5$ (Sanders et al. 2021), and potentially beyond (Cucchiara et al. 2015; Faisst et al. 2016; Jones et al. 2020).

3.1. Galaxy Sample Compilation

For the main analysis, a survey for [C II] emission in main-sequence galaxies at $z \sim 2$ (Zanella et al. 2018) is included to represent [C II]-emitting star-forming galaxies at this epoch. At higher redshifts, $z \sim 4-6$, we make use of the recent ALMA Large Program to Investigate C+ at Early Times (ALPINE) survey (Le

Fèvre et al. 2020; Béthermin et al. 2020; Faisst et al. 2020; Fujimoto et al. 2020), which includes measurements of the [C II] line emission and kinematics, and physical galaxy properties based on extensive UV to submillimeter data. Supplementing this survey, we include an additional sample of galaxies at $z \sim 5$ –6 from Capak et al. (2015). The full high-redshift sample is comprised of main-sequence star-forming galaxies with stellar masses in the range of $M_* = 10^{9.5} - 10^{11} M_\odot$, SFRs of ≈ 5 to $600 M_\odot \text{ yr}^{-1}$, and gas-phase metallicities $12 + \log(\text{O}/\text{H}) = 8.12$ to 8.77 ($Z = 0.3$ – $1.2 Z_\odot$).

Due to the accessibility of the 21 cm line transition as a tracer of H I in the local universe, these observations are utilized here to represent the H I gas content of galaxies at $z = 0$. As the reference sample at $z \sim 0$, we adopt the combined catalog of galaxies from The H I Nearby Galaxy Survey (THINGS; Walter et al. 2008) and the HERA CO-Line Extragalactic Survey (HERACLES; Leroy et al. 2008). This sample includes galaxies with stellar masses, SFRs, and atomic and molecular hydrogen gas mass estimates. Importantly, it includes galaxies with mass ranges similarly distributed as those in the high- z sample compilation. For consistency, the FMR is used to compute the gas-phase metallicity for each system, yielding metal abundances in the range of $12 + \log(\text{O}/\text{H}) = 8.6$ – 8.8 (i.e., 80%–125% solar abundance). In our analysis, we also include the recent estimates of the average H I gas content at $z \approx 1$ – 1.3 (Chowdhury et al. 2020, 2021), based on stacking of the H I 21 cm signal of a large ensemble of star-forming galaxies. This work provides measurements of M_{HI} and ρ_{HI} intermediate to the galaxy samples at $z \sim 0$ and $z \gtrsim 2$ examined here.

For the compiled set of [C II]-emitting galaxies at $z = 2$ – 6 we infer H I gas masses in the range of $M_{\text{HI}} = 3 \times 10^9 - 2 \times 10^{11} M_\odot$. At redshifts ≈ 1 and above, all galaxies are observed to have H I gas masses in excess of their stellar mass M_* , contrasting the low H I content in nearby galaxies (see Figure 3). The high-redshift H I mass estimates are consistent with the inferred excess of the total ISM mass for galaxies in a similar stellar mass range (typically by a factor of 2–3 over the stellar mass; e.g., Scoville et al. 2017), the first indication that H I dominates the total ISM mass of galaxies at $z \gtrsim 2$.

3.2. Evolution of the H I Gas Fraction with Redshift

With estimates of the H I content in galaxies from $z \approx 6$ to the present, we first quantify the redshift evolution of the H I gas fraction, M_{HI}/M_* . The full compiled data set is shown in Figure 4, where the H I gas fraction is observed to increase from $M_{\text{HI}}/M_* = 0.37^{+0.42}_{-0.29}$ (1σ confidence interval of the sample distribution) at $z = 0$ to $M_{\text{HI}}/M_* = 6.79^{+1.45}_{-5.27}$ at $z \sim 4$ – 6 . Coupling the $z \sim 0$ – 1 data based on 21 cm observations of H I with the new measurements based on the [C II]-to-H I conversion factor we observe a steady increase of M_{HI}/M_* as a function of redshift. Equivalently, the fraction of H I, $f_{\text{HI}} = M_{\text{HI}}/(M_{\text{HI}} + M_*)$, is observed to constitute $\approx 70\%$ at $z \sim 4$ – 6 , decreasing to $f_{\text{HI}} \approx 25\%$ at $z = 0$.

We confirm the determined redshift evolution of the H I gas fraction by constructing a simple model using literature scaling relations. Here, we subtract the measured average trend of M_{H_2}/M_* (i.e., $M_{\text{H}_2}/M_* \propto (1+z)^{2.3}$; Carilli & Walter 2013; Tacconi et al. 2018) from the measured evolution of the total ISM mass (i.e., $M_{\text{gas}} = M_{\text{H}_2} + M_{\text{HI}}$), prescribed as $M_{\text{gas}}/M_* \propto (1+z)^{1.84}$ (Scoville et al. 2017). This yields a function of the

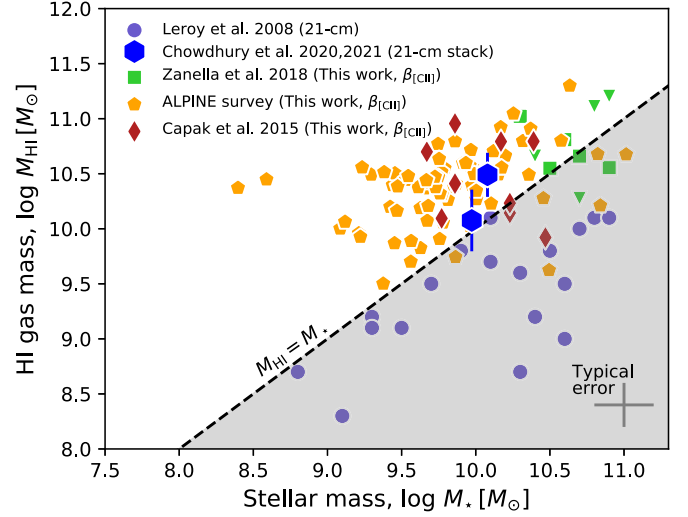


Figure 3. H I gas mass and stellar mass distributions. The compiled galaxy samples are shown as a function of redshift, with distinct symbols and colors. The new measurements of the H I gas masses at $z > 2$ were derived using the [C II]-to-H I conversion factor from Figure 2, based on high-redshift [C II]-emitting galaxy samples: green: Zanella et al. (2018), yellow: the ALPINE survey (Le Fèvre et al. 2020; Béthermin et al. 2020; Faisst et al. 2020), and red: Capak et al. (2015). Lower redshift measurements come from 21 cm observations: purple: Leroy et al. (2008, $z \approx 0$) and blue: Chowdhury et al. (2020, 2021, $z \approx 1$). The dashed line represents $M_{\text{HI}} = M_*$, clearly separating galaxies with H I gas masses in excess (majority at $z \gtrsim 1$) or in deficit ($z \sim 0$) of the stellar mass.

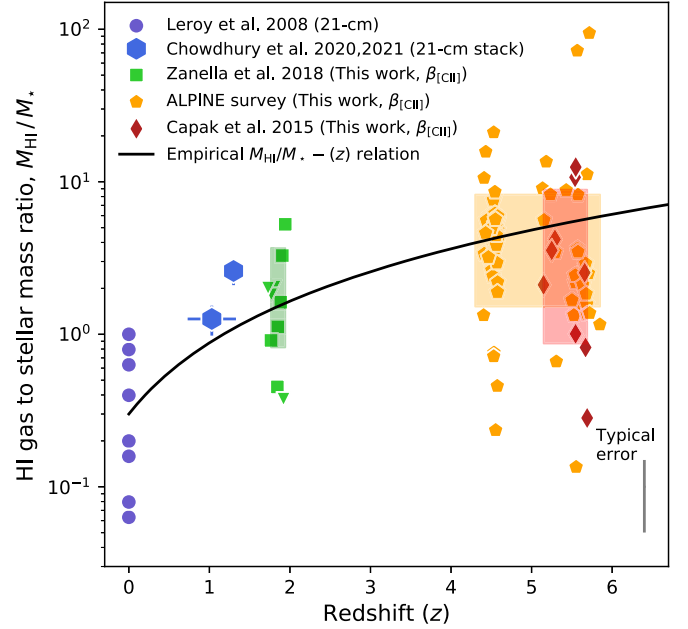


Figure 4. Redshift evolution of the H I gas mass of star-forming galaxies. Symbol notations follow those in Figure 3. Colored boxes mark the 16th–84th confidence interval of M_{HI}/M_* and span the full redshift distribution for each high-redshift sample. The black curve shows the expected evolution of $M_{\text{HI}}/M_*(z)$ based on independent empirical scaling relations (see the text).

form

$$\frac{M_{\text{HI}}}{M_*} = 0.4 \times (1+z)^{1.84} \left[1 - \frac{(1+z)^{0.46}}{4} \right] \quad (3)$$

based on the observed ratio $M_{\text{H}_2} = 1/3 M_{\text{HI}}$ for the reference sample at $z = 0$, shown in Figure 4. This expression can be

approximated by $M_{\text{HI}}/M_* = 0.3 \times (1+z)^{1.55}$. The strong correspondence between the inferred trend in this simple model and our measurements is striking. We note that this observed trend indicates that H I is more abundant than H₂ at all redshifts, when compared to the evolution of M_{H_2}/M_* with redshift (e.g., Geach et al. 2011; Carilli & Walter 2013; Tacconi et al. 2018).

Moreover, while not directly measurable from the available data, we can still provide an approximate estimate of the fraction of H I to the total baryonic mass (i.e., $M_{\text{bar,tot}} = M_{\text{HI}} + M_{\text{H}_2} + M_*$) from these relations. Starting from $M_{\text{H}_2} = 1/3 M_{\text{HI}}$ at $z=0$ and accounting for the predicted redshift evolution of $M_{\text{H}_2}/M_{\text{HI}} \propto (1+z)^{-0.34}$ (Morselli et al. 2021), we estimate $M_{\text{HI}}/M_{\text{bar,tot}} \approx 60\%$ at $z \sim 4-6$, which decreases to $\approx 20\%$ at $z=0$. We obtain similar results if we instead adopt the [C II]-to-H₂ scaling from Zanella et al. (2018) to additionally compute M_{H_2} . Based on this and the results above, H I is thus observed to dominate the baryonic matter content of star-forming galaxies at $z \gtrsim 2$.

Finally, while [C II] is now being increasingly detected in emission, well into the epoch of reionization at $z \gtrsim 7$ (e.g., Knudsen et al. 2017; Bradač et al. 2017; Smit et al. 2018; Hashimoto et al. 2019; Fujimoto et al. 2019), we refrain from including these systems in the main analysis due to the lack of well-defined samples surveying [C II] at these redshifts. The [C II]-to-H I conversion factor derived is still applicable for these distant galaxies though. For a few of the individual [C II] emitters detected at $z \sim 7$ (Knudsen et al. 2017; Smit et al. 2018), we infer H I masses exceeding the stellar mass by a factor of ≈ 10 , consistent with the measured redshift evolution of the M_{HI}/M_* ratio.

3.3. Metallicity Dependence of the H I Gas Fraction

In addition to examining the evolution of the H I gas fraction with redshift, here we quantify whether the high-redshift measurements follow the observed anticorrelation with gas-phase metallicity observed in the local universe (Hughes et al. 2013; Brown et al. 2018; Stark et al. 2021). At fixed redshifts, this is equivalently represented as a decrease in the H I fraction with increasing stellar mass (Catinella et al. 2013; Brown et al. 2015). In Figure 5 we show the gas fraction M_{HI}/M_* as a function of metal abundance $12 + \log(\text{O}/\text{H})$ for each galaxy in our compiled high- z sample. For comparison, we overplot the extended GALEX Arcibo SDSS Survey (xGASS) catalog of galaxies at $z \sim 0$ with direct H I 21 cm observations (Catinella et al. 2018), together with the empirical relation derived for the H I Mapping Nearby Galaxies at Apache Point Observatory (MaNGA) sample galaxies (Stark et al. 2021). The combined sample of galaxies, spanning redshifts from $z=0-6$, is observed to closely follow this local, empirical relation.

This establishes the relation between the gas fraction M_{HI}/M_* and $12 + \log(\text{O}/\text{H})$ as fundamental. Moreover, it further substantiates the empirical [C II]-to-H I conversion factor derived here and validates the inferred H I gas masses of the high-redshift galaxy samples.

3.4. H I Depletion Times

With the inferred H I gas masses, we can also estimate the H I depletion times, $t_{\text{dep,HI}} = M_{\text{HI}}/\text{SFR}$, of each galaxy, which provide the timescale on which H I would be exhausted by star formation. This estimate is independent of whether the neutral gas has to first be converted to H₂ or can form stars directly

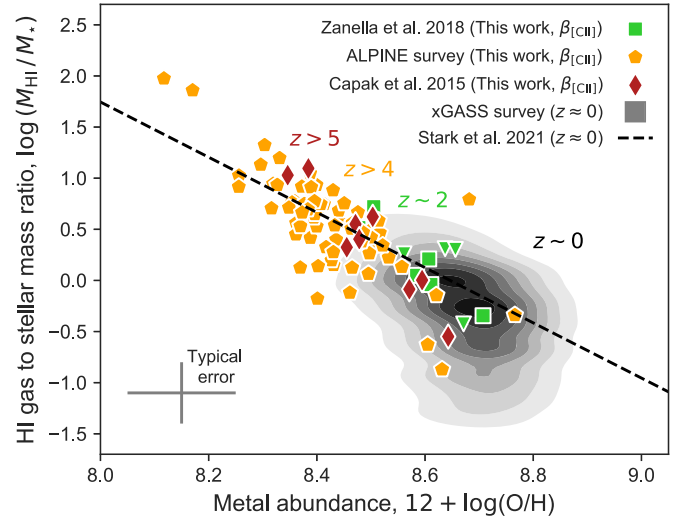


Figure 5. Metallicity evolution of the H I gas fraction, M_{HI}/M_* . Symbol notations follow those in Figure 3. Metal abundances are determined for each high-redshift galaxy based on the FMR (Curti et al. 2020). The xGASS catalog of galaxies at $z \sim 0$ with direct H I 21 cm observations (Catinella et al. 2018) is shown as the gray shaded contours for comparison, together with the empirical relation derived for the H I MaNGA sample galaxies (Stark et al. 2021; black dashed line). Both nearby and distant galaxies, at $z=0-6$, are observed to follow this fundamental relation.

from the available neutral gas. At $z \sim 0$, star-forming galaxies typically have H I depletion times $t_{\text{dep,HI}} \approx 5$ Gyr, significantly longer than the H₂ depletion times observed for the same galaxies ($t_{\text{dep,H}_2} \lesssim 1$ Gyr; Saintonge et al. 2017). At $z \approx 1$, $t_{\text{dep,HI}}$ decreases to an average about 1.5 Gyr (Chowdhury et al. 2020).

In Figure 6, we explore the H I depletion timescales for the high-redshift galaxy samples, including the lower redshift comparison samples with direct H I 21 cm measurements. As already hinted by the $z \approx 1-1.3$ measurements from Chowdhury et al. (2020, 2021), we confirm a continued decrease of $t_{\text{dep,HI}}$ at $z \gtrsim 2$. At these redshifts, the majority of galaxies show H I depletion times $\lesssim 2$ Gyr. This indicates that at least for the first four billion years of cosmic time, the H I gas reservoirs in galaxies have to be constantly replenished to fuel the high star formation activity. When this infall of neutral gas is discontinued, the available gas will be exhausted due to the short H I depletion timescales at $z \gtrsim 2$, thereby quenching the ongoing star formation as a result.

3.5. Comparison to the Dynamical Mass

To further explore the contribution of M_{HI} to the total ISM mass budget in high-redshift galaxies, we here compare our measurements to the dynamical mass M_{dyn} estimates of each galaxy. Assuming that the [C II] emission originates from a rotation-dominated disk we infer M_{dyn} within the [C II]-emitting region determined from the individual line widths. We determine this as $M_{\text{dyn}} = 1.16 \times 10^5 v_{\text{cir}}^2 D$, with D as the disk diameter and $v_{\text{cir}} = 0.75 \text{FWHM}_{[\text{CII}]} / \sin(i)$ (Wang et al. 2013). For the cases where the inclination angle i of the galaxy is not available, we assume $i = 55^\circ$ (Wang et al. 2013; Willott et al. 2015). The dynamical masses are shown in Figure 7, in comparison to the H I gas mass. For the $z \sim 2$ galaxy sample, M_{dyn} is on average ≈ 3 times higher than M_{HI} , consistent with a larger contribution from the molecular gas and stellar mass components in galaxies at these redshifts. The galaxies at $z \gtrsim 4$,

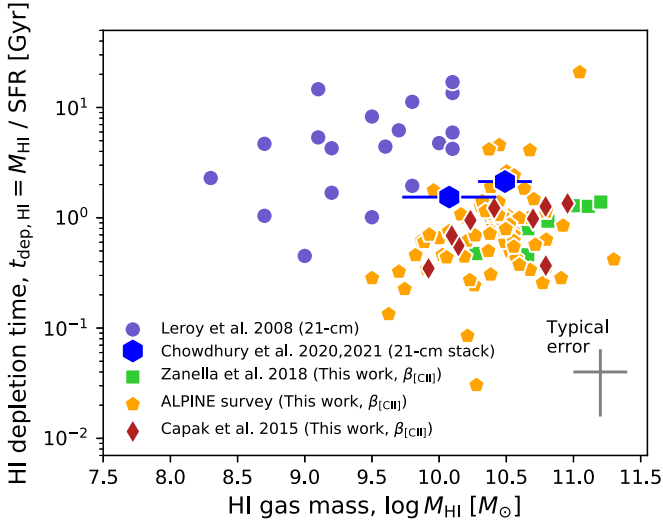


Figure 6. H I depletion time of star-forming galaxies. Symbol notations follow those in Figure 3. Galaxies at $z \sim 0$ have available neutral gas reservoirs to maintain star formation for ≈ 1 –10 Gyr. The majority of galaxies at higher redshifts have H I depletion times $\lesssim 2$ Gyr.

however, on average show dynamical masses consistent with the inferred H I mass.

We note that Dessauges-Zavadsky et al. (2020) found consistent results between the molecular gas masses inferred for a subset of the ALPINE sample and the total dynamical mass after accounting for the stellar mass contribution. However, these estimates are based on the $\alpha_{\text{[CII]}}$ calibration derived for solar-metallicity galaxies at $z \approx 2$ by Zanella et al. (2018), which have not been verified for high-redshift galaxies with lower gas-phase metallicities. It is clear though that the atomic and molecular gas potentially both present a large mass fraction.

These considerations and the results above are yet more evidence indicating that H I dominates the baryonic matter content of galaxies at this epoch. Moreover, these results lend further credibility to the accuracy of the [C II]-to-H I calibration, demonstrating that it can recover sensible values over a large mass range.

4. The Cosmic H I Gas Mass Density

The cosmic density of neutral atomic gas associated with galaxies (ρ_{HI}) is an important parameter in understanding the baryon cycle of galaxies. In the local universe, ρ_{HI} can be derived from 21 cm H I observations of individual galaxies (Zwaan et al. 2005; Hoppmann et al. 2015; Jones et al. 2018). This method can be extended to $z \approx 1$ by considering an ensemble of galaxies, i.e., via stacking (Chowdhury et al. 2020). At higher redshifts, $z \gtrsim 2$, ρ_{HI} has been measured from quasar absorption spectroscopy of DLA systems (Péroux et al. 2003; Prochaska & Wolfe 2009; Noterdaeme et al. 2012; Neeleman et al. 2016). DLAs only probe random sightlines through their associated galaxy counterparts, however, and are increasingly difficult to detect at $z \gtrsim 4$ due to the blanketing effect of the Ly α forest. In most cases, DLA sightlines also only recover the extended H I envelope of their associated galaxies rather than the gas responsible for star formation (Neeleman et al. 2019; see also Section 2.3).

The [C II]-to-H I conversion factor derived here allows us to measure ρ_{HI} directly from the star-forming gas in galaxies at $z \approx 2$ and beyond. To do this, we derive the [C II] luminosity

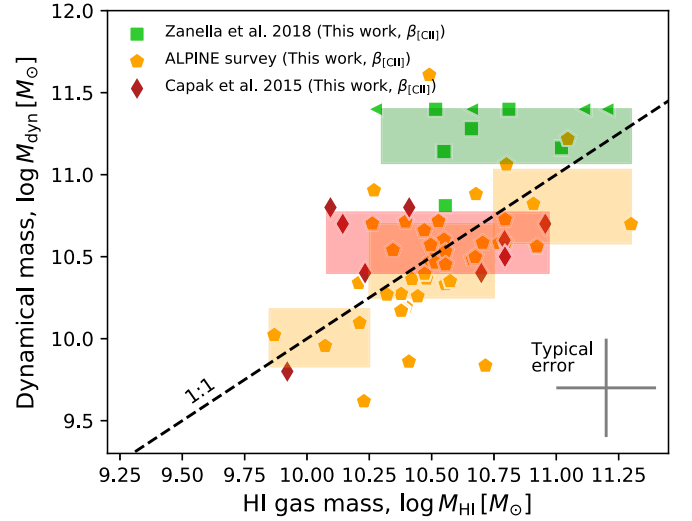


Figure 7. Comparison of the dynamical mass and H I gas mass estimated from the [C II] line. Boxes mark vertically the 16th–84th percentile on the dynamical mass distribution of each subsample and horizontally the H I gas mass interval. The colors of the boxes correspond to the samples they represent. The general good consistency between M_{dyn} and M_{HI} of the galaxies at $z \gtrsim 4$ indicates that the H I gas contributes dominantly to the overall dynamic mass within the [C II]-emitting region. Galaxies at $z \sim 2$ show larger dynamical masses than the H I component, possibly due to larger contributions from the molecular gas and stellar component at this epoch.

density, $\mathcal{L}_{\text{[CII]}}$, by integrating over the entire luminosity function $\mathcal{L}_{\text{[CII]}} = \int_{L_{\text{[CII]}}}^{\infty} L_{\text{[CII]}} \phi(L_{\text{[CII]}}) dL_{\text{[CII]}}$. We separate the analysis into three sample redshifts: $z = 4$ –6, $z = 2$, and $z = 0$. This is to account for the evolution in the luminosity function of [C II] and the overall increase in the metal abundance of typical galaxies across cosmic time. A similar approach is commonly used to determine the H_2 gas mass density in galaxies $\rho_{\text{H}_2}(z)$ based on the relevant CO luminosity function and a CO-to- H_2 conversion factor (Walter et al. 2014; Decarli et al. 2016, 2019, 2020; Riechers et al. 2019). At the highest redshifts, $z = 4$ –6, we adopt the [C II] luminosity function from the ALPINE survey (Yan et al. 2020). This yields a luminosity density of $\mathcal{L}_{\text{[CII]}} = 2.8 \times 10^6 L_{\odot} \text{Mpc}^{-3}$. To infer the equivalent cosmic H I gas mass density in galaxies, the average metallicity $12 + \log(\text{O}/\text{H}) = 8.4$ (i.e., $\log(Z/Z_{\odot}) = -0.3$) observed for the sample galaxies at the same redshift is used to determine the relevant conversion factor of $\beta_{\text{[CII]}} = 55^{+18}_{-13} M_{\odot}/L_{\odot}$. This yields $\rho_{\text{HI}} = 1.6^{+0.5}_{-0.4} \times 10^8 M_{\odot} \text{Mpc}^{-3}$ at $z \sim 4$ –6. Since the infrared luminosity function, which is connected to [C II], shows little evolution from $z = 6$ to $z \approx 2$ (Gruppioni et al. 2020; Loiacono et al. 2021), we adopt the same [C II] luminosity density above to estimate ρ_{HI} at $z = 2$. However, since the average metal abundance of galaxies increases with decreasing redshift, a higher average metallicity is required to determine the appropriate $\beta_{\text{[CII]}}$ calibration. Based on the average gas-phase metallicity of $12 + \log(\text{O}/\text{H}) = 8.6$ (i.e., $\log(Z/Z_{\odot}) = -0.1$) for the subset of galaxies at $z \approx 2$, we derive a conversion factor of $\beta_{\text{[CII]}} = 37^{+12}_{-9} M_{\odot}/L_{\odot}$. This results in $\rho_{\text{HI}} = 1.0^{+0.3}_{-0.3} \times 10^8 M_{\odot} \text{Mpc}^{-3}$ at $z = 2$, consistent (within 1σ) with the results at $z \sim 4$ –6. Due to a significant evolution of the [C II] luminosity function from $z = 6$ to the present, the more appropriate function from Hemmati et al. (2017) is adopted at $z \sim 0$. Integrating this yields a luminosity density of $\mathcal{L}_{\text{[CII]}} = 1.0 \times 10^6 L_{\odot} \text{Mpc}^{-3}$. At solar abundances, the average inferred for the subset of galaxies at

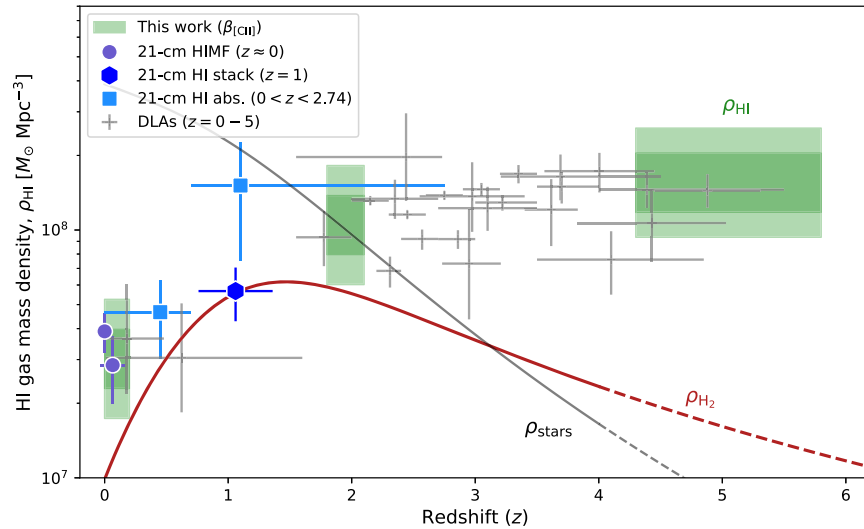


Figure 8. Redshift evolution of the cosmic H I gas mass density in galaxies ρ_{HI} . Measurements from this work are based on the estimated [C II] luminosity densities at each sample redshift, converted to ρ_{HI} (see the text). The vertical dark and light green regions encompass the 68% and 95% confidence levels, respectively, of the ρ_{HI} measurements and horizontally indicate redshift intervals. The gray dots at $z \sim 0$ show measurements of ρ_{HI} based on H I mass functions from recent 21 cm observations (Hoppmann et al. 2015; Jones et al. 2018) and the large hexagon shows the average measurement of an ensemble of galaxies at $z \approx 1$ (Chowdhury et al. 2020). Blue squares show the results from a survey of intervening 21-cm H I absorption systems covering $0 < z < 0.69$ and $0.69 < z < 2.74$ (Grasha et al. 2020). Gray crosses represent DLA measurements (Walter et al. 2020), corrected by 20% to account for the contribution from sub-DLAs and Lyman-limit systems. Our measurements are consistent with these other recent estimates and indicate (at $\approx 3\sigma$ significance) a decrease of ρ_{HI} in galaxies by a factor of ≈ 5 from $z \sim 4$ –6 to the present. For comparison, the evolution of the cosmic density of stars (Madau & Dickinson 2014) and the molecular gases in galaxies are shown as well, extrapolated beyond $z > 4$ from the analysis of Walter et al. (2020).

$z \approx 0$, the [C II]-to-H I conversion factor is $\beta_{[\text{CII}]} = 30_{-7}^{+10}$. This translates to a local measurement of $\rho_{\text{HI}} = 3.0_{-0.7}^{+1.0} \times 10^7 M_{\odot} \text{Mpc}^{-3}$.

Figure 8 shows the measured redshift evolution of $\rho_{\text{HI}}(z)$. For comparison, we only include the most recent estimates of ρ_{HI} derived from H I 21 cm observations of local galaxies (Hoppmann et al. 2015; Jones et al. 2018). We note that previous estimates from 21 cm observations seem to systematically recover higher values of ρ_{HI} at $z \sim 0$ (e.g., Lah et al. 2007; Braun 2012). The most recent 21 cm measurements, however, are also in the best agreement with low-redshift DLA measurements (Neeleman et al. 2016; Shull et al. 2017), so we only consider these for the main analysis. In the figure we also include the inferred average value of $\rho_{\text{HI}} = (6.75 \pm 1.65) \times 10^7 M_{\odot} \text{Mpc}^{-3}$ in star-forming galaxies at $z \approx 1$ from Chowdhury et al. (2020). We also show the results from Grasha et al. (2020), surveying 21-cm H I absorption systems at $z \sim 0$ –3 in addition to the DLA sample compiled by including ρ_{HI} measurements covering $z \sim 0$ –5 from previous works (Péroux et al. 2003; Prochaska & Wolfe 2009; Guimarães et al. 2009; Crighton et al. 2015), but here corrected by 20% to account for the contribution to the cosmic H I budget from sub-DLAs and Lyman-limit systems (O’Meara et al. 2007; Noterdaeme et al. 2012; Zafar et al. 2013; Berg et al. 2019).

We observe that the H I density in galaxies shows a negligible decrease in the first ≈ 4 Gyr after the Big Bang, from $z \approx 6$ to $z = 2$. At this point, coincident with the peak of cosmic SFR density, the cosmic H I mass density declines substantially by a factor of ≈ 5 to the present. This decline is a factor of ≈ 2 larger than previously inferred (e.g., Walter et al. 2020; Péroux & Howk 2020). In contrast, the stellar mass density in galaxies ρ_{stars} increases by a factor of ≈ 50 during the same cosmic time span. Intriguingly, at $z = 0$, ρ_{stars} exceeds the sum of the baryonic densities at $z = 6$, suggesting continued accretion of gas onto galaxies from outside the regions we

measure with [C II]. The significant decrease in ρ_{HI} (and ρ_{H_2}), however, indicates that the neutral atomic gas in galaxies begins to be exhausted at this point. The paucity of continuous H I gas infall and accretion, required to replenish the available gas reservoirs, is thus not sufficient to fuel and maintain star formation following the peak of the cosmic SFR density. These results further support a decreasing fraction of $\rho_{\text{H}_2}/(\rho_{\text{H}_2} + \rho_{\text{HI}})$ beyond $z \approx 2$ (Walter et al. 2020), reaching 10% at $z \sim 4$ –6. This is contrary to recent results suggesting an increase in the molecular to total ISM gas fraction (Sommovigo et al. 2021).

Finally, we can also make a simple prediction of the redshift evolution of ρ_{HI} based on these new data points. A simple function of the form $\rho_{\text{HI}}(z) = 3 \times 10^7 (1 + z)^{0.85} M_{\odot} \text{Mpc}^{-3}$ (or equivalently $\Omega_{\text{HI}}(z) = 2 \times 10^{-4} (1 + z)^{0.85}$) is found to represent the data well. Notably, this predicts a significant decrease in $\rho_{\text{HI}}(z)$, with a value at $z = 0$ that is approximately a factor of 2 lower than previously inferred (Walter et al. 2020; Péroux & Howk 2020).

5. Summary and Outlook

This work provides the first direct calibration of the conversion between the [C II] line luminosity $L_{[\text{CII}]}$ and the H I gas mass M_{HI} for high-redshift galaxies, denoted here as $\beta_{[\text{CII}]} \equiv M_{\text{HI}}/L_{[\text{CII}]}$. The atomic gas-phase in the ISM of galaxies at these epochs is otherwise undetectable due to the weakness of the typically employed tracer, the fine-structure 21 cm H I transition, which only allows observations of individual galaxies out to $z \approx 0.4$ (Fernández et al. 2016) or $z \approx 1$ by combining the signals from thousands of galaxies (Chowdhury et al. 2020) with current radio observatories.

We applied this calibration to existing samples of [C II]-emitting galaxies at $z \approx 2$ –6 to quantify the evolution of the H I gas content in galaxies through cosmic time. We found that the H I gas fraction, M_{HI}/M_{\star} , increases continuously as a function of redshift, with M_{HI} exceeding M_{\star} at $z \approx 1$. The H I gas

fraction was found to similarly be dependent on the gas-phase metallicity, $12 + \log(\text{O}/\text{H})$, following a universal anticorrelation from $z = 0$ to $z = 6$. Comparing the inferred H I gas masses to the measured SFRs of each galaxy, we uncovered that the majority of galaxies at $z \gtrsim 2$ have H I depletion timescales, $t_{\text{dep,H I}} = M_{\text{H I}}/\text{SFR}$, less than ≈ 2 Gyr, substantially shorter than observed in galaxies at $z \approx 0$. This we argued indicates that the atomic gas reservoirs are required to be constantly replenished at $z \gtrsim 2$ to fuel the high star formation activity. We further compared the inferred H I gas masses to the total dynamical masses M_{dyn} derived from the individual line widths within the [C II]-emitting region. At $z \sim 4\text{--}6$, $M_{\text{H I}}$ was found to be consistent with M_{dyn} on average, suggesting that H I dominates the total ISM mass budget at this epoch, whereas a larger contribution to M_{dyn} from other components, likely the molecular gas, was evident in galaxies at $z \approx 2$.

We further used the $\beta_{[\text{C II}]}$ calibration to determine the comoving mass density of H I in galaxies as a function of redshift $\rho_{\text{H I}}(z)$. This was based on measurements of the [C II] luminosity density $\mathcal{L}_{[\text{C II}]}$ at three distinct epochs, $z = 0$, $z = 2$, and $z = 4\text{--}6$, using previously constrained luminosity functions, which can be converted into $\rho_{\text{H I}}$. We measured $\rho_{\text{H I}} = 1.6^{+0.5}_{-0.4} \times 10^8 M_{\odot} \text{Mpc}^{-3}$ at $z \sim 4\text{--}6$, a factor of ≈ 5 larger than at $z = 0$. These measurements were consistent with previous estimates using DLAs. We emphasize, however, that the $\beta_{[\text{C II}]}$ calibration has the potential to infer $\rho_{\text{H I}}$ far beyond current estimates, well into the epoch of reionization at $z \approx 7$.

As already demonstrated by surveys targeting CO and [C I] as tracers of the molecular gas content, the use of the [C II]-to-H I conversion factor derived here is similarly important to advance our understanding of the atomic gas content in high-redshift galaxies. Even with next generation radio observatories, such as the Square Kilometer Array (SKA), the H I 21 cm transition might only be detected for individual galaxies out to $z \approx 1.7$ (Blyth et al. 2015), further motivating the development and use of alternative tracers. We encourage follow-up observations and simulations to further substantiate the [C II]-to-H I conversion derived here.


We would like to thank the referee for the constructive feedback on the analysis and presentation of the results in this work. We thank Johan P. U. Fynbo and J. Xavier Prochaska for insightful discussions during an early stage of this project. We thank Karen P. Olsen for early access to the simulated galaxy data set. We thank Marcel Neeleman for providing us the DLA sample compilation. K.E.H. acknowledges support by a Postdoctoral Fellowship Grant (217690–051) from The Icelandic Research Fund. D.W. is supported by Independent Research Fund Denmark grant DFF–7014–00017. The Cosmic Dawn Center is supported by the Danish National Research Foundation under grant No. 140. D.N. acknowledges support from the U.S. NSF via grant AAG–1909153.

Data Availability Statement

The European Southern Observatory (ESO) Very Large Telescope/X-shooter GRB afterglow spectra are all publicly available through the ESO archive in the form of phase 3 material. The ALMA–ALPINE catalog is available at https://cesam.lam.fr/a2c2s/data_release.php. The open-source code VoigtFit used to model the absorption-line features is available at <https://github.com/jkrogager/VoigtFit>. Source

codes for the figures and tables presented in this manuscript are available from the corresponding author upon reasonable request.

ORCID iDs

Kasper E. Heintz  <https://orcid.org/0000-0002-9389-7413>
 Darach Watson  <https://orcid.org/0000-0002-4465-8264>
 Pascal A. Oesch  <https://orcid.org/0000-0001-5851-6649>
 Desika Narayanan  <https://orcid.org/0000-0002-7064-4309>
 Suzanne C. Madden  <https://orcid.org/0000-0003-3229-2899>

References

- Appleton, P. N., Guillard, P., Boulanger, F., et al. 2013, *ApJ*, **777**, 66
 Asplund, M., Grevesse, N., Sauval, A. J., & Scott, P. 2009, *ARA&A*, **47**, 481
 Berg, T. A. M., Ellison, S. L., Sánchez-Ramírez, R., et al. 2019, *MNRAS*, **488**, 4356
 Béthermin, M., Fudamoto, Y., Ginolfi, M., et al. 2020, *A&A*, **643**, A2
 Blyth, S., van der Hulst, T. M., Verheijen, M. A. W., et al. 2015, in Proc. of Advancing Astrophysics with the Square Kilometre Array (AASKA14) (Trieste: PoS), **128**
 Bolatto, A. D., Wolfire, M., & Leroy, A. K. 2013, *ARA&A*, **51**, 207
 Bolmer, J., Ledoux, C., Wiseman, P., et al. 2019, *A&A*, **623**, A43
 Bradač, M., García-Appadoo, D., Huang, K.-H., et al. 2017, *ApJL*, **836**, L2
 Braun, R. 2012, *ApJ*, **749**, 87
 Brown, T., Catinella, B., Cortese, L., et al. 2015, *MNRAS*, **452**, 2479
 Brown, T., Cortese, L., Catinella, B., & Kilborn, V. 2018, *MNRAS*, **473**, 1868
 Capak, P. L., Carilli, C., Jones, G., et al. 2015, *Natur*, **522**, 455
 Carilli, C. L., & Walter, F. 2013, *ARA&A*, **51**, 105
 Carniani, S., Maiolino, R., Smit, R., & Amorín, R. 2018, *ApJL*, **854**, L7
 Catinella, B., Schiminovich, D., Cortese, L., et al. 2013, *MNRAS*, **436**, 34
 Catinella, B., Saintonge, A., Janowiecki, S., et al. 2018, *MNRAS*, **476**, 875
 Chowdhury, A., Kanekar, N., Chengalur, J. N., Sethi, S., & Dwarakanath, K. S. 2020, *Natur*, **586**, 369
 Chowdhury, A., Kanekar, N., Das, B., Dwarakanath, K. S., & Sethi, S. 2021, *ApJL*, **913**, L34
 Christensen, L., Fynbo, J. P. U., Prochaska, J. X., et al. 2011, *ApJ*, **727**, 73
 Christensen, L., Møller, P., Fynbo, J. P. U., & Zafar, T. 2014, *MNRAS*, **445**, 225
 Cormier, D., Madden, S. C., Lebouteiller, V., et al. 2015, *A&A*, **578**, A53
 Cormier, D., Abel, N. P., Hony, S., et al. 2019, *A&A*, **626**, A23
 Crighton, N. H. M., Murphy, M. T., Prochaska, J. X., et al. 2015, *MNRAS*, **452**, 217
 Croxall, K. V., Smith, J. D., Pellegrini, E., et al. 2017, *ApJ*, **845**, 96
 Cucchiara, A., Fumagalli, M., Rafelski, M., et al. 2015, *ApJ*, **804**, 51
 Curti, M., Mannucci, F., Cresci, G., & Maiolino, R. 2020, *MNRAS*, **491**, 944
 De Cia, A., Ledoux, C., Mattsson, L., et al. 2016, *A&A*, **596**, A97
 Decarli, R., Aravena, M., Boogaard, L., et al. 2020, *ApJ*, **902**, 110
 Decarli, R., Walter, F., Aravena, M., et al. 2016, *ApJ*, **833**, 69
 Decarli, R., Walter, F., González-López, J., et al. 2019, *ApJ*, **882**, 138
 Dessauges-Zavadsky, M., Ginolfi, M., Pozzi, F., et al. 2020, *A&A*, **643**, A5
 Díaz-Santos, T., Armus, L., Charmandaris, V., et al. 2017, *ApJ*, **846**, 32
 Faist, A. L., Capak, P. L., Davidzon, I., et al. 2016, *ApJ*, **822**, 29
 Faist, A. L., Schaerer, D., Lemaux, B. C., et al. 2020, *ApJS*, **247**, 61
 Fernández, X., Gim, H. B., van Gorkom, J. H., et al. 2016, *ApJL*, **824**, L1
 Franeck, A., Walch, S., Seifried, D., et al. 2018, *MNRAS*, **481**, 4277
 Fujimoto, S., Ouchi, M., Ferrara, A., et al. 2019, *ApJ*, **887**, 107
 Fujimoto, S., Silverman, J. D., Béthermin, M., et al. 2020, *ApJ*, **900**, 1
 Fynbo, J. P. U., Jakobsson, P., Prochaska, J. X., et al. 2009, *ApJS*, **185**, 526
 Fynbo, J. P. U., Starling, R. L. C., Ledoux, C., et al. 2006, *A&A*, **451**, L47
 Geach, J. E., Smail, I., Moran, S. M., et al. 2011, *ApJL*, **730**, L19
 Gehrels, N., Chincarini, G., Giommi, P., et al. 2004, *ApJ*, **611**, 1005
 Grasha, K., Darling, J., Leroy, A. K., & Bolatto, A. D. 2020, *MNRAS*, **498**, 883
 Greiner, J., Fox, D. B., Schady, P., et al. 2015, *ApJ*, **809**, 76
 Grupponi, C., Béthermin, M., Loiacono, F., et al. 2020, *A&A*, **643**, A8
 Guimarães, R., Petitjean, P., de Carvalho, R. R., et al. 2009, *A&A*, **508**, 133
 Harikane, Y., Ouchi, M., Inoue, A. K., et al. 2020, *ApJ*, **896**, 93
 Harrington, K. C., Weiss, A., Yun, M. S., et al. 2021, *ApJ*, **908**, 95
 Hashimoto, T., Inoue, A. K., Mawatari, K., et al. 2019, *PASJ*, **71**, 71
 Heintz, K. E., Bolmer, J., Ledoux, C., et al. 2019, *A&A*, **629**, A131

- Heintz, K. E., & Watson, D. 2020, [ApJL](#), **889**, L7
- Hemmati, S., Yan, L., Diaz-Santos, T., et al. 2017, [ApJ](#), **834**, 36
- Herrera-Camus, R., Förster Schreiber, N., Genzel, R., et al. 2021, [A&A](#), **649**, A31
- Hoppmann, L., Staveley-Smith, L., Freudling, W., et al. 2015, [MNRAS](#), **452**, 3726
- Hughes, T. M., Cortese, L., Boselli, A., Gavazzi, G., & Davies, J. I. 2013, [A&A](#), **550**, A115
- Jakobsson, P., Fynbo, J. P. U., Ledoux, C., et al. 2006, [A&A](#), **460**, L13
- Jakobsson, P., Hjorth, J., Fynbo, J. P. U., et al. 2004, [A&A](#), **427**, 785
- Jones, M. G., Haynes, M. P., Giovanelli, R., & Moorman, C. 2018, [MNRAS](#), **477**, 2
- Jones, T., Sanders, R., Roberts-Borsani, G., et al. 2020, [ApJ](#), **903**, 150
- Knudsen, K. K., Watson, D., Frayer, D., et al. 2017, [MNRAS](#), **466**, 138
- Krogager, J.-K. 2018, arXiv:1803.01187
- Krogager, J. K., Fynbo, J. P. U., Møller, P., et al. 2012, [MNRAS](#), **424**, L1
- Krogager, J. K., Møller, P., Fynbo, J. P. U., & Noterdaeme, P. 2017, [MNRAS](#), **469**, 2959
- Lah, P., Chengalur, J. N., Briggs, F. H., et al. 2007, [MNRAS](#), **376**, 1357
- Le Fèvre, O., Béthermin, M., Faisst, A., et al. 2020, [A&A](#), **643**, A1
- Leroy, A. K., Walter, F., Brinks, E., et al. 2008, [AJ](#), **136**, 2782
- Loiacono, F., Decarli, R., Gruppioni, C., et al. 2021, [A&A](#), **646**, A76
- Madau, P., & Dickinson, M. 2014, [ARA&A](#), **52**, 415
- Madden, S. C., Cormier, D., Hony, S., et al. 2020, [A&A](#), **643**, A141
- Madden, S. C., Poglitsch, A., Geis, N., Stacey, G. J., & Townes, C. H. 1997, [ApJ](#), **483**, 200
- Madden, S. C., Rémy-Ruyer, A., Galametz, M., et al. 2013, [PASP](#), **125**, 600
- Magdis, G. E., Daddi, E., Béthermin, M., et al. 2012, [ApJ](#), **760**, 6
- Morselli, L., Renzini, A., Enia, A., & Rodighiero, G. 2021, [MNRAS](#), **502**, L85
- Neeleman, M., Kanekar, N., Prochaska, J. X., Rafelski, M. A., & Carilli, C. L. 2019, [ApJL](#), **870**, L19
- Neeleman, M., Prochaska, J. X., Ribaud, J., et al. 2016, [ApJ](#), **818**, 113
- Neeleman, M., Prochaska, J. X., & Wolfe, A. M. 2015, [ApJ](#), **800**, 7
- Noterdaeme, P., Petitjean, P., Carithers, W. C., et al. 2012, [A&A](#), **547**, L1
- O'Meara, J. M., Prochaska, J. X., Burles, S., et al. 2007, [ApJ](#), **656**, 666
- Palmerio, J. T., Vergani, S. D., Salvaterra, R., et al. 2019, [A&A](#), **623**, A26
- Papadopoulos, P. P., Thi, W. F., & Viti, S. 2004, [MNRAS](#), **351**, 147
- Pardos Olsen, K., Burkhart, B., Mac Low, M.-M., et al. 2021, arXiv:2102.02868
- Perley, D. A., Tanvir, N. R., Hjorth, J., et al. 2016, [ApJ](#), **817**, 8
- Péroux, C., Bouché, N., Kulkarni, V. P., York, D. G., & Vladilo, G. 2011, [MNRAS](#), **410**, 2237
- Péroux, C., & Howk, J. C. 2020, [ARA&A](#), **58**, 363
- Péroux, C., McMahon, R. G., Storrie-Lombardi, L. J., & Irwin, M. J. 2003, [MNRAS](#), **346**, 1103
- Pineda, J. L., Langer, W. D., & Goldsmith, P. F. 2014, [A&A](#), **570**, A121
- Popping, G., Narayanan, D., Somerville, R. S., Faisst, A. L., & Krumholz, M. R. 2019, [MNRAS](#), **482**, 4906
- Prochaska, J. X., Chen, H.-W., Dessauges-Zavadsky, M., & Bloom, J. S. 2007, [ApJ](#), **666**, 267
- Prochaska, J. X., & Wolfe, A. M. 2009, [ApJ](#), **696**, 1543
- Rahmani, H., Péroux, C., Turnshek, D. A., et al. 2016, [MNRAS](#), **463**, 980
- Ramos Padilla, A. F., Wang, L., Ploekinger, S., van der Tak, F. F. S., & Trager, S. C. 2021, [A&A](#), **645**, A133
- Rémy-Ruyer, A., Madden, S. C., Galliano, F., et al. 2014, [A&A](#), **563**, A31
- Rhodin, N. H. P., Christensen, L., Møller, P., Zafar, T., & Fynbo, J. P. U. 2018, [A&A](#), **618**, A129
- Riechers, D. A., Pavesi, R., Sharon, C. E., et al. 2019, [ApJ](#), **872**, 7
- Robertson, B. E., & Ellis, R. S. 2012, [ApJ](#), **744**, 95
- Saintonge, A., Catinella, B., Tacconi, L. J., et al. 2017, [ApJS](#), **233**, 22
- Sanders, R. L., Shapley, A. E., Jones, T., et al. 2021, [ApJ](#), **914**, 19
- Scoville, N., Aussel, H., Sheth, K., et al. 2014, [ApJ](#), **783**, 84
- Scoville, N., Lee, N., Vanden Bout, P., et al. 2017, [ApJ](#), **837**, 150
- Scoville, N., Sheth, K., Aussel, H., et al. 2016, [ApJ](#), **820**, 83
- Selsing, J., Malesani, D., Goldoni, P., et al. 2019, [A&A](#), **623**, A92
- Shull, J. M., Danforth, C. W., Tilton, E. M., Moloney, J., & Stevans, M. L. 2017, [ApJ](#), **849**, 106
- Simcoe, R. A., Onoue, M., Eilers, A.-C., et al. 2020, arXiv:2011.10582
- Smit, R., Bouwens, R. J., Carniani, S., et al. 2018, [Natur](#), **553**, 178
- Sommovigo, L., Ferrara, A., Carniani, S., et al. 2021, [MNRAS](#), **503**, 4878
- Speagle, J. S., Steinhardt, C. L., Capak, P. L., & Silverman, J. D. 2014, [ApJS](#), **214**, 15
- Stark, D. V., Masters, K. L., Avila-Reese, V., et al. 2021, [MNRAS](#), **503**, 1345
- Tacconi, L. J., Genzel, R., & Sternberg, A. 2020, [ARA&A](#), **58**, 157
- Tacconi, L. J., Genzel, R., Neri, R., et al. 2010, [Natur](#), **463**, 781
- Tacconi, L. J., Genzel, R., Saintonge, A., et al. 2018, [ApJ](#), **853**, 179
- Tanvir, N. R., Levan, A. J., Fruchter, A. S., et al. 2012, [ApJ](#), **754**, 46
- Tarantino, E., Bolatto, A. D., Herrera-Camus, R., et al. 2021, [ApJ](#), **915**, 92
- Valentino, F., Daddi, E., Puglisi, A., et al. 2020, [A&A](#), **641**, A155
- Valentino, F., Magdis, G. E., Daddi, E., et al. 2018, [ApJ](#), **869**, 27
- Vreeswijk, P. M., Ellison, S. L., Ledoux, C., et al. 2004, [A&A](#), **419**, 927
- Walter, F., Brinks, E., de Blok, W. J. G., et al. 2008, [AJ](#), **136**, 2563
- Walter, F., Carilli, C., Neeleman, M., et al. 2020, [ApJ](#), **902**, 111
- Walter, F., Decarli, R., Sargent, M., et al. 2014, [ApJ](#), **782**, 79
- Walter, F., Weiß, A., Downes, D., Decarli, R., & Henkel, C. 2011, [ApJ](#), **730**, 18
- Wang, R., Wagg, J., Carilli, C. L., et al. 2013, [ApJ](#), **773**, 44
- Willott, C. J., Bergeron, J., & Omont, A. 2015, [ApJ](#), **801**, 123
- Wolfe, A. M., Gawiser, E., & Prochaska, J. X. 2005, [ARA&A](#), **43**, 861
- Wolfe, A. M., Prochaska, J. X., & Gawiser, E. 2003, [ApJ](#), **593**, 215
- Woosley, S. E., & Bloom, J. S. 2006, [ARA&A](#), **44**, 507
- Yan, L., Sajina, A., Loiacono, F., et al. 2020, [ApJ](#), **905**, 147
- Zafar, T., Péroux, C., Popping, A., et al. 2013, [A&A](#), **556**, A141
- Zanella, A., Daddi, E., Magdis, G., et al. 2018, [MNRAS](#), **481**, 1976
- Zwaan, M. A., Meyer, M. J., Staveley-Smith, L., & Webster, R. L. 2005, [MNRAS](#), **359**, L30